

PAPER

## Diffractive elements with multi-ring spectra

To cite this article: Saifollah Rasouli *et al* 2025 *J. Opt.* **27** 045602

View the [article online](#) for updates and enhancements.

### You may also like

- [Additive engineering of nonlinear optical properties of all-inorganic halide perovskites](#)  
Ali Fatemi, Kazem Jamshidi-Ghaleh, Tavakkol Tohidi et al.
- [Kerr self-focusing of few-cycle terahertz pulses in dispersive media](#)  
Jieya Ruan, Guoqian Liao, Tingting Xi et al.
- [Stochastic Stokes origami: folds, cusps and skyrmionic facets in random polarisation fields](#)  
Kerr Maxwell and Mark R Dennis

# Diffractive elements with multi-ring spectra

Saifollah Rasouli<sup>1,2,3,\*</sup> , Davud Hebri<sup>4</sup>, Seyed Mohammad Hasan Narimani<sup>1,5</sup> and Sergey A Ponomarenko<sup>6,4</sup>

<sup>1</sup> Department of Physics, Institute for Advanced Studies in Basic Sciences (IASBS), Zanjan 45137-66731, Iran

<sup>2</sup> Center for International Scientific Studies and Collaboration (CISSC), Ministry of Science, Research and Technology, Tehran 15875-7788, Iran

<sup>3</sup> Optics Research Center, Institute for Advanced Studies in Basic Sciences (IASBS), Zanjan 45137-66731, Iran

<sup>4</sup> Department of Physics and Atmospheric Science, Dalhousie University, Halifax, Nova Scotia B3H 4R2, Canada

<sup>5</sup> Department of Physics, University of Isfahan, Isfahan 81746-73441, Iran

<sup>6</sup> Department of Electrical and Computer Engineering, Dalhousie University, Halifax, Nova Scotia B3J 2X4, Canada

E-mail: [rasouli@iasbs.ac.ir](mailto:rasouli@iasbs.ac.ir)

Received 17 December 2024, revised 23 January 2025

Accepted for publication 7 February 2025

Published 18 February 2025



## Abstract

We introduce pure amplitude almost periodic structures (APSs) with multi-ring spatial spectra, characterized by four degrees of freedom in the spectral domain: the number of rings, the number of impulses on each ring, the radius of each ring, and the angular positions of the impulses within a ring. A comprehensive mathematical framework is developed to describe the diffraction of arbitrary optical beams by such structures. This framework is theoretically validated and experimentally verified through the analysis of diffraction patterns produced under Gaussian beam illumination. The method is systematically tested on various APS configurations, including structures with one, two, three, and four rings, as well as different impulse arrangements within these rings, demonstrating its robustness and adaptability. Notably, each APS achieves a high diffraction efficiency, transferring approximately  $1/((2N+1)(2N))$  of the transmitted beam power to each impulse, where  $2N$  represents the total number of impulses excluding the zero-diffraction order. This efficiency is significantly superior to that of conventional spatial light modulators. Additionally, a detailed comparison between theoretical predictions and experimental measurements of power ratios for the diffraction orders confirms the accuracy and reliability of our approach. The versatility of APS makes them highly suitable for a range of applications, including optical communications, optical tweezing, multi-particle trapping, screening, micro-manipulation, and microscopy. For example, APS-enhanced Gaussian lattice beams can improve imaging speed in fluorescence microscopy. Furthermore, their ability to enable three-dimensional optical multiple trapping and beam splitting positions APS as a powerful tool for advancing laser and optical research.

\* Author to whom any correspondence should be addressed.

Supplementary material for this article is available [online](#)

Keywords: almost periodic structures (APSs), diffractive optical elements (DOEs), beam splitting, optical beam diffraction

## 1. Introduction

Guiding and splitting optical beams with precision has been among objectives in optics. Historically, a mirror represents one of the earliest tools used to alter a light path through reflection. Humans have also long understood the principles of refraction, especially when light passes from one transparent medium to another at angles below the critical angle. The interplay of reflection and refraction of a light beam transmitted through an optical plate allows for simultaneous manipulation of light. When the reflection and transmission coefficients are equal, thereby balanced beam splitter divides a light beam into equal beamlets. Optical plates and gratings were among the first elements specifically designed for this purpose.

The concept of the diffraction grating dates back to around 1785, when David Rittenhouse, an inventor from Philadelphia, created the first artificial grating by stringing hairs between finely threaded screws [1]. This invention paved the way for Joseph von Fraunhofer's notable wire diffraction grating in 1821 [2]. Diffractive optical elements (DOEs), which are designed to divide an input beam into multiple replicas, have become integral to various optical applications, including image processing and communications, among others. DOEs play a crucial role in modern optics, enabling precise control over light for diverse applications such as microscopy, structured beam generation, optical communications, holography, and optical trapping [3–6]. Among the various types of DOEs, periodic structures have been widely studied and utilized. DOEs achieve desired light patterns by altering a phase and/or amplitude of incident wavefront. These elements can perform optical functions that would be difficult or impossible with conventional optics, such as beam shaping, dividing, pattern generation, and light diffusion. For an in-depth discussion of DOEs, their design principles, and applications, readers can refer to [7, 8]. However, the limitations imposed by DOE periodicity, such as fixed diffraction angles and restricted flexibility in creating complex patterns, have spurred researchers to explore alternatives.

Generic multi-beam dividers, which are widely used in applications such as material processing, interferometry, image processing, and optical communications [9], present a viable alternative. Research on these devices began with Dammann gratings and efforts to optimize their efficiency [10]. For instance, a closed-form expression for the optimal one-dimensional (1D) phase triplicator was derived using the calculus of variations [11]. Subsequent work led to closed-form solutions for optimal phase duplicators with specific power ratios and for four-beam dividers [12]. The generalization of these results to higher-order beam dividers of both 1D and 2D varieties was explored by Romero and Dickey

in a series of influential papers [13], later summarized in a broader context of beam shaping [14]. Significant recent advancements in both theoretical and experimental aspects are reported in [15], with asymmetric spatial power dividers using phase–amplitude metasurfaces being particularly noteworthy [16]. Beam dividers are foundational elements for more sophisticated forms of optical processing, both in theory and in practice. Recently, affine diffractive beam dividers have also been introduced [17]. Another important research direction is splitting of structured light beams; numerous techniques were proposed to this end, including the use of two-level pure-phase DOEs [18]. Recent advancements in DOEs have demonstrated their potential for efficient beam sorting in applications such as orbital angular momentum multiplexing, with compact designs and high-resolution fabrication techniques achieving excellent performance in terms of efficiency, fidelity, and low cross-talk [19].

In this work, we introduce a class of DOEs that belong to a class of almost periodic structures (APSs). The introduced structures are defined by their spatial spectra, consisting of regularly spaced impulses arranged on multiple concentric circles. The design parameters include the number of rings, the number of impulses per ring, the radius of each ring, and the relative rotation of impulses on different rings, denoted as  $(M, N_m, \nu_m, \alpha_m)$ . We demonstrate the versatility of these designs through examples of APS structures with double-, triple-, and quadruple-ring spectra. We advance a general mathematical framework to describe the diffraction of any optical beam by such structures and study diffraction of Gaussian beams in detail. We show that at a sufficiently large distance from the structure or near the focal plane of a Fourier lens, the Gaussian beam diffraction pattern exhibits  $2N$  high-intensity Gaussian beamlets carrying equal power. This feature indicates the potential of the introduced APSs for three-dimensional optical multiple trapping.

## 2. Almost-periodic structures: a concise review

Almost periodic functions are significant extensions of the periodic functions. Danish mathematician Harald Bohr [20] established the theory of almost periodic functions in 1923, which was subsequently expanded upon by Besicovitch and Besicovitch [21] and other researchers. In optics, APSs arise as structures with almost periodic transmittance  $t_{\text{APS}}(\mathbf{r})$  which can be represented by a 2D generalized Fourier series as [6, 22–24]:

$$t_{\text{APS}}(\mathbf{r}) = \sum_{n=0}^{\infty} t_n e^{i2\pi \mathbf{f}_n \cdot \mathbf{r}}, \quad (1)$$

where  $\mathbf{r} = (x, y) = (r \cos \theta, r \sin \theta)$  is the position vector in a transverse plane;  $t_n$  stands for a Fourier coefficient and  $\mathbf{f}_n = (f_{nx}, f_{ny})$  represents an arbitrary point in the spectral domain. For  $n = 0$  (zero diffraction order),  $\mathbf{f}_0 = (f_{0x}, f_{0y}) = (0, 0)$  indicates the central impulse located at the origin of the spectral domain. We can evaluate the Fourier coefficient as [22]:

$$t_n = \lim_{L \rightarrow \infty} \frac{1}{L^2} \int_{-L/2}^{L/2} \int_{-L/2}^{L/2} \exp(-i\mathbf{k}_{\perp n} \cdot \mathbf{r}) t_{\text{APS}}(\mathbf{r}) dx dy, \quad (2)$$

where  $\mathbf{k}_{\perp n} = 2\pi \mathbf{f}_n$ . The spatial spectrum of an APS then reads [22, 23]:

$$T_{\text{APS}}(\xi, \eta) = \sum_{n=0}^{\infty} t_n \delta(\xi - f_{nx}, \eta - f_{ny}), \quad (3)$$

where  $\delta(\dots)$  is an (impulse) delta function in the spectral domain. Hence, an APS has a discrete spatial spectrum, but the individual impulses can be neither identical nor regularly spaced. Let an APS located in  $z = 0$  plane be illuminated by a plane wave of wavelength  $\lambda$  propagating along the  $z$  axis. The amplitude of a diffracted wave is then

$$\Psi(\mathbf{r}, z) \propto \sum_{n=0}^{\infty} t_n e^{i\mathbf{k}_n \cdot \mathbf{r}}, \quad (4)$$

where  $\mathbf{k}_n = (\mathbf{k}_{\perp n}, k_{zn})$ , so that  $k_{zn} = 2\pi \sqrt{\lambda^{-2} - (f_{nx}^2 + f_{ny}^2)}$ . Near-field diffraction of a plane wave from APSs has been studied in [23]. The study reveals that if the APS spectrum consists of impulses on zone-plate-like concentric circles, the structure exhibits self-images under plane wave illumination.

Suppose the APS is illuminated by an arbitrary optical beam with a complex envelope  $u(\mathbf{r}, 0)$ . Right past the APS, the beam envelope reads

$$\Psi(\mathbf{r}, 0) = u(\mathbf{r}, 0) t_{\text{APS}}(\mathbf{r}), \quad (5)$$

while at a distance  $z$  past the APS it is [6, 24]

$$\Psi(\mathbf{r}, z) = e^{ikr^2/2z} \sum_{n=0}^{\infty} t_n e^{-ikr_n^2/2z} u(\mathbf{r}_n, z). \quad (6)$$

Here  $k = 2\pi/\lambda$  and  $\mathbf{r}_n = \mathbf{r} - \lambda z \mathbf{f}_n$  is a radius vector in the coordinate frame with the origin shifted to the center of the  $n$ th diffraction order. Equation (6) implies that an APS can be considered as a hologram that multiplies replicas of the incident beam. Further, we can show that the ratio of the  $n$ th diffraction order power to the total transmitted power is given by [6, 24]

$$\frac{P_n}{P_{\text{tr}}} = \frac{|t_n|^2}{\sum_{n=0}^{\infty} |t_n|^2}. \quad (7)$$

### 3. Single-ring-spectrum elements

Consider a single-ring-spectrum APS described in appendix of [23]. This optical element was used for three-dimensional multiple particle trapping in [6]. In this case, the impulses are placed at both the center and vertices of an octagon in the spectral domain. Expanding on this concept, the novel APS can be constructed with the spectral impulses located at the center and vertices of a regular polygon [24]. We can express the transmittance of such an element as

$$t_{2N}(\mathbf{r}) = \frac{1}{2} + \frac{1}{2N} \sum_{n=1}^N \cos(2\pi \mathbf{f}_n \cdot \mathbf{r}), \quad (8)$$

where  $\mathbf{f}_n = (\nu \cos \varphi_n, \nu \sin \varphi_n)$  with  $\varphi_n = (n-1)\frac{\pi}{N}$  and  $\nu$  being the fundamental (spatial) frequency of the structure. Although the structure defined by equation (8) is not generally periodic, we can define a characteristic fundamental quasi-period of the structure,  $\Lambda = \nu^{-1}$ . We sketch the spectrum of a typical single-ring structure in figure 1(a).

To facilitate a direct comparison with the general form of APSs, equation (1), we can rewrite equation (8) as

$$t_{2N}(\mathbf{r}) = \frac{1}{2} + \frac{1}{4N} \sum_{n=1}^{2N} \exp(i2\pi \mathbf{f}_n \cdot \mathbf{r}), \quad (9)$$

where we used  $\mathbf{f}_{N+m} = -\mathbf{f}_m$  for  $m = 1, 2, \dots, N$  as a result of  $\varphi_{N+m} = \varphi_m + \pi$ . Comparing equations (1) and (9) we conclude that  $t_0 = 1/2$ ,  $t_n = (4N)^{-1}$  for  $1 \leq n \leq 2N$ , and  $t_n = 0$  otherwise. On substituting these Fourier coefficients and  $\mathbf{f}_n$  into equation (6), we obtain [24]

$$\Psi(\mathbf{r}, z) = \frac{1}{2} u(\mathbf{r}, z) + \frac{e^{-i2\pi z/z_T}}{4N} \sum_{n=1}^{2N} e^{i2\pi \nu r \cos(\theta - \varphi_n)} u(\mathbf{r}_n, z), \quad (10)$$

where  $z_T = 2\Lambda^2/\lambda$  indicates the Talbot distance for arbitrary beam diffracted from a single-ring structure.

We now specify to the incident Gaussian beam. The complex amplitude of the latter at the distance  $z$  is [25]

$$u_G(r, z) = \frac{w_0}{w(z)} e^{-\frac{r^2}{w^2(z)}} e^{i[kz + \frac{\pi r^2}{2R(z)} - \zeta(z)]}, \quad (11)$$

where  $w_0$  is a spot size and

$$w(z) = w_0 \sqrt{1 + (z/z_R)^2}, \quad (12a)$$

$$R(z) = z \left[ 1 + (z_R/z)^2 \right], \quad (12b)$$

$$\zeta(z) = \tan^{-1}(z/z_R), \quad (12c)$$

$$z_R = \pi w_0^2/\lambda. \quad (12d)$$

Here  $w(z)$  is a beam width,  $\zeta(z)$  Gouy phase shift, and  $z_R$  Rayleigh length at the distance  $z$ . Let a Gaussian beam with

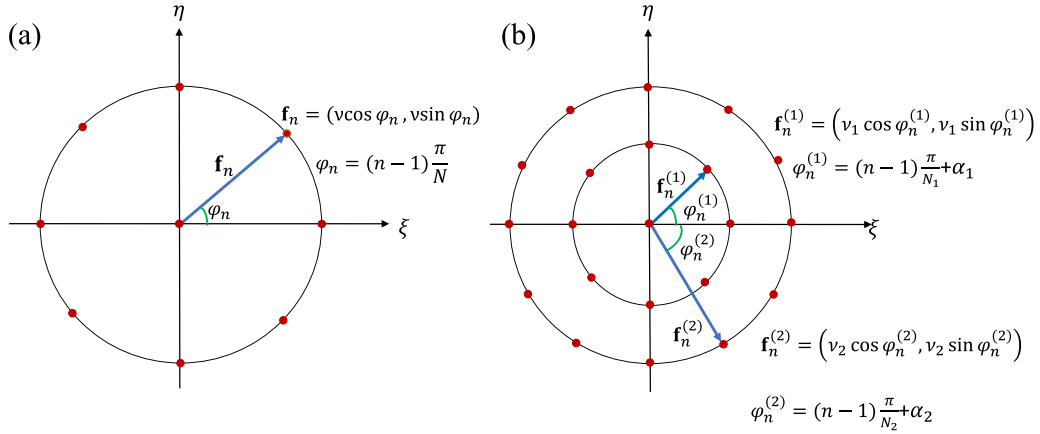


**Figure 1.** Impulse comb of two typical multi-ring APS in the spectral domain: (a) single-ring structure with  $N = 4$  (b) double-ring APS with  $N_1 = 4$  and  $N_2 = 6$ .

its waist at  $z = 0$  illuminate a single-ring APS. We can express the complex amplitude of the diffracted beam as

$$\Psi(\mathbf{r}, z) = \frac{1}{2} u_G(r, z) + \frac{e^{-i2\pi z/z_T}}{4N} \sum_{n=1}^{2N} e^{i2\pi \nu r \cos(\theta - \varphi_n)} u_G(r_n, z), \quad (13)$$

where we employed equation (10). It follows from equation (13) that the diffracted beam is a superposition of  $2N + 1$  individual Gaussians, which share the same characteristics as the incident beam and their centers are distributed along a circle of radius  $R_c = \lambda z \nu$  as well as at the circle center. We can express the ratio of  $R_c$  to the beam radius as

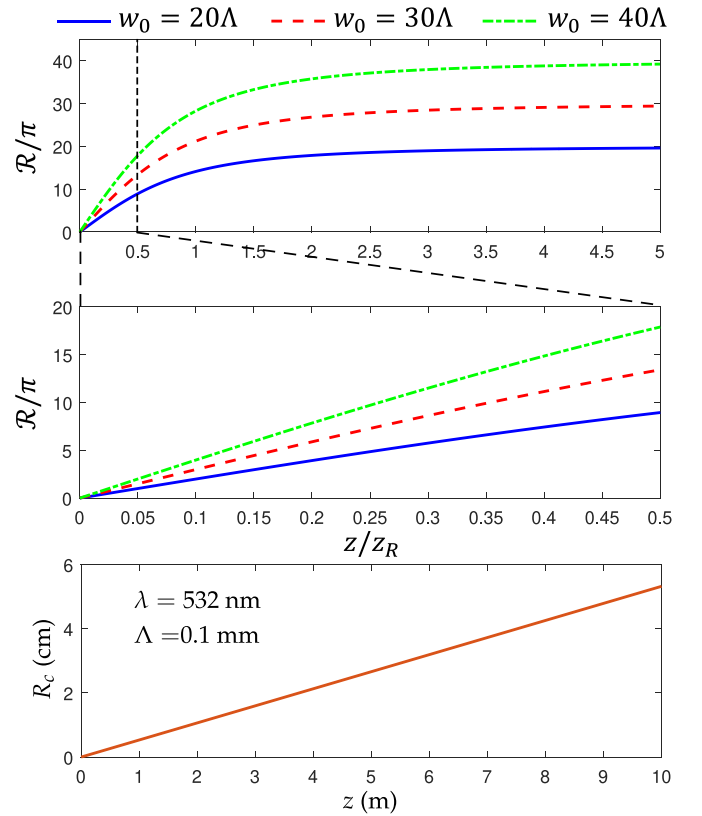
$$\mathcal{R} = \frac{R_c}{w(z)} = \frac{\pi w_0}{\Lambda} \frac{z/z_R}{\sqrt{1 + (z/z_R)^2}}. \quad (14)$$

In the near-field regime,  $z \ll z_R$ , we have  $\mathcal{R} = \lambda z / (w_0 \Lambda)$ . Conversely, in the far-field regime,  $z \gg z_R$ ,  $\mathcal{R} \simeq \pi w_0 / \Lambda$ . In figure 2, We display  $\mathcal{R}$  as function of  $z$  for variable  $w_0/\Lambda$  in figure 2. We can infer from the figure that  $\mathcal{R}$  increases with the propagation distance in the far-field region.

We can estimate the propagation distance over which distinct diffraction orders separate by equating the perimeter of the circular array,  $2\pi R_c$ , to  $2N \times 2w_0$ . It follows that

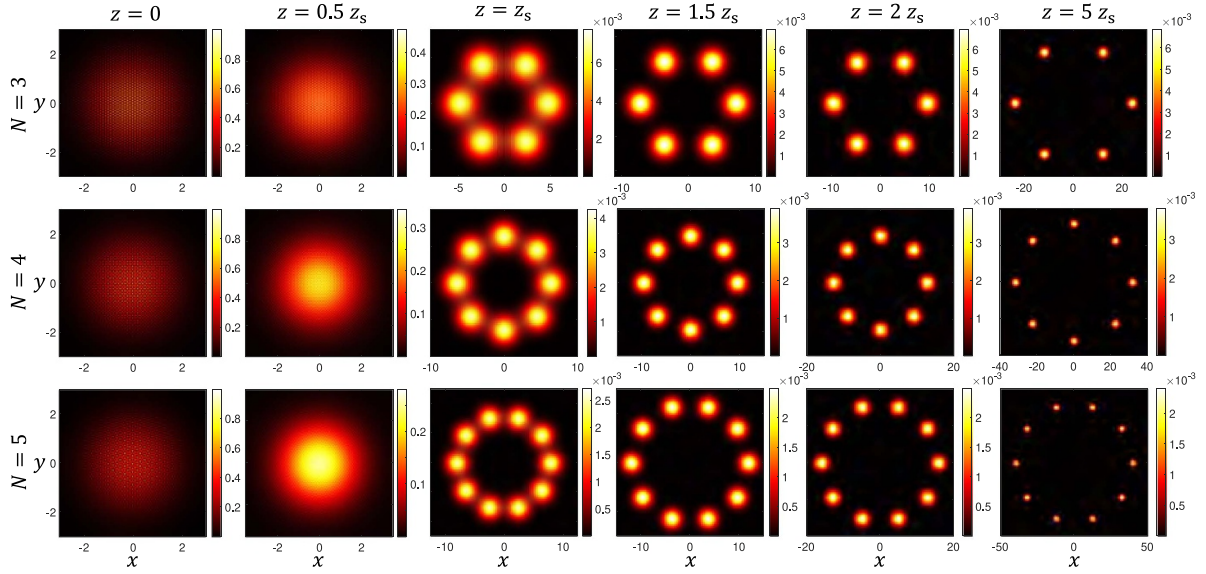
$$z_s = \frac{2N\Lambda w_0}{\pi \lambda}. \quad (15)$$

Figure 3 illustrates diffraction of a Gaussian beam by three distinct single-ring structures. As anticipated, diffraction orders spatially separate after the propagation distance of  $z_s$ . The diffracted intensities are normalized to the peak incident intensity on the structures, resulting in color bars with a maximum value of one immediately past the structures. During propagation, various diffraction orders adopt the spatial profile of the incident beam but travel in different directions, resulting in their angular separation. Initially, the intensity maxima of these orders decrease as the transmitted power is distributed among them. Over longer propagation distances, the diffraction orders move further apart, eventually reaching distances



**Figure 2.** Top and middle rows: the ratio of the radius of the circular array to the beam radius,  $\mathcal{R} = R_c/w(z)$ , versus  $z/z_R$  for variable  $w_0/\Lambda$ . Bottom row: the radius of the circular array in terms of propagation distance.

greater than their own dimensions or those of the incident beam. As soon as this condition is met, the intensity maxima of the diffraction orders stabilize and remain constant up to a propagation distance shorter than the Rayleigh length. However, when the propagation distance exceeds the Rayleigh length of each diffracted beam, the spatial extent of the beams increases, resulting in a decrease in their maximum intensities on farther propagation.



**Figure 3.** Diffraction patterns of some single-ring APS structures with  $\Lambda = 0.1$  mm and different values of  $N$  illuminated by a Gaussian beam with  $\lambda = 532$  nm and  $w_0 = 2.5$  mm. The central diffraction order has been removed to increase the visibility of other diffraction orders.

#### 4. Multi-ring APSs

By extending the concept to multi-ring spectral structures, we can introduce another family of APSs with regularly spaced spectral impulses located on multiple concentric rings. For instance, we sketch the spectrum of a double-ring in figure 1(b). We can express the transmittance function of a generic multi-ring APS as

$$t_{2N}^{(M)}(\mathbf{r}) = \frac{1}{2} + \frac{1}{2N} \sum_{m=1}^M \sum_{n=1}^{2N_m} \cos(2\pi \mathbf{f}_n^{(m)} \cdot \mathbf{r}), \quad (16)$$

where  $M$  stands for the number of spectral rings; the number of impulses over the  $m$ th ring equals to  $2N_m$ , and  $N = N_1 + N_2 + \dots + N_M$  so that the total number of impulses, excluding the zero diffraction order, is  $2N$ . Further,  $\mathbf{f}_n^{(m)} = (\nu_m \cos \varphi_n^{(m)}, \nu_m \sin \varphi_n^{(m)})$  with  $\varphi_n^{(m)} = (n-1)\frac{\pi}{N_m} + \alpha_m$  and  $\nu_m$  denoting the radius of the  $m$ th ring in the spectral domain of the structure. Although the structure defined by equation (16) is not generally periodic, we can again define a quasi-period  $\Lambda_m = \nu_m^{-1}$  of the  $m$ th ring. To compare with the general form of APS, we rewrite equation (16) as

$$t_{2N}^{(M)}(\mathbf{r}) = \frac{1}{2} + \frac{1}{4N} \sum_{m=1}^M \sum_{n=1}^{2N_m} \exp(i2\pi \mathbf{f}_n^{(m)} \cdot \mathbf{r}). \quad (17)$$

On comparing equations (17) and (1), we infer that  $t_0 = \frac{1}{2}$ ,  $t_n = \frac{1}{4N}$  for  $1 \leq n \leq 2N$ , and  $t_n = 0$  for  $n > 2N$ ;  $2N + 1 = 2 \sum_{m=1}^M N_m + 1$  equals to the total number of impulses. In this case, the power APS transmission coefficient reads  $P_{tr}/P_{in} = (2N + 1)/(8N)$ . In figure 4 we show the transmitted power as function of  $N$ . As is apparent, the power transmission coefficient decreases with  $N$ , approaching 25%. We separate the transmitted power into two parts:  $P_0$ , associated with the zero

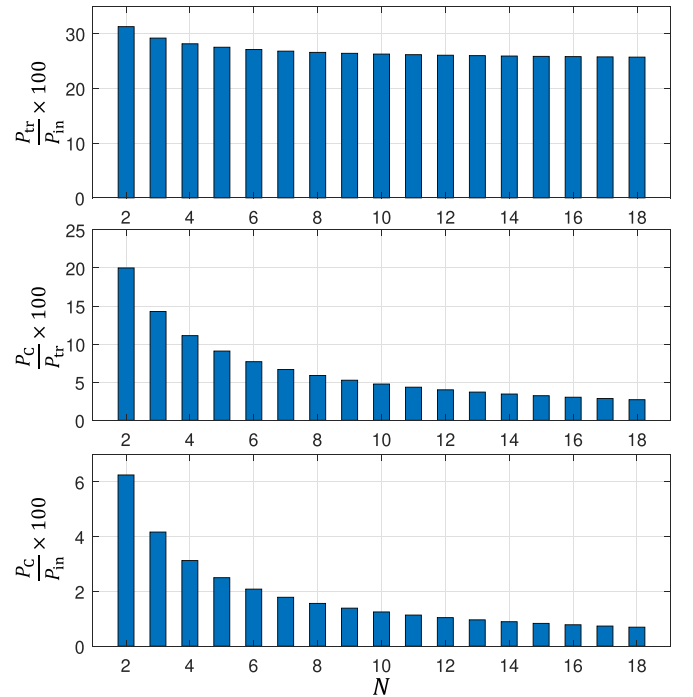


**Figure 4.** Power transmittance of multi-ring APS as a function of  $N$  (top row). Distribution of total power share of impulses on concentric circles from transmitted power (middle row) and incident power (bottom row).

diffraction order or impulse, and  $P_C$ , representing the total power of other impulses on the concentric circles. We can show that the power fractions of zero-order impulse and others relative to the transmitted power are  $P_0/P_{tr} = 2N/(2N + 1)$  and  $P_C/P_{tr} = 1/(2N + 1)$ , respectively. Further, the power fractions of the zero-order and the others are  $P_0/P_{in} = 1/4$  and  $P_C/P_{in} = 1/(8N)$ .

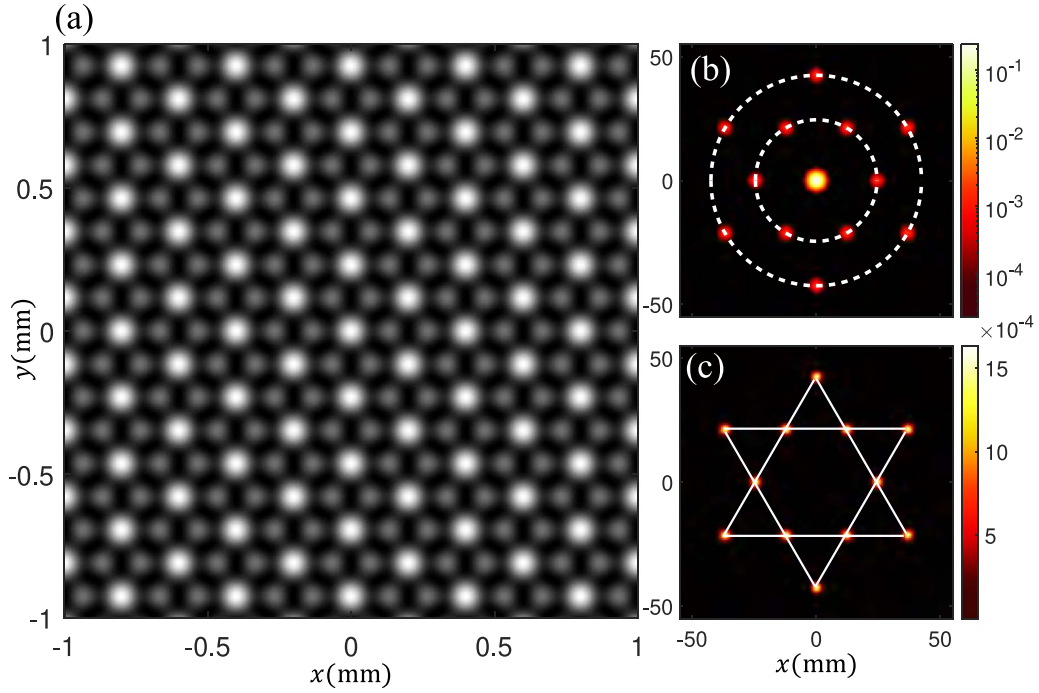


**Figure 5.** (a) Transmission function of a double-ring APS with  $N_1 = N_2 = 3$ ,  $\Lambda_2 = \Lambda_1/\sqrt{3}$ ,  $\alpha_1 = 0$ , and  $\alpha_2 = \pi/6$ . (b) and (c) Diffraction pattern of a Gaussian beam with  $\lambda = 532$  nm and  $w_0 = 2.5$  mm at a distance  $z = z_R/4$  from this structure. In (b) a logarithmic color scale is used and in (c) the central diffraction order has been removed to increase the visibility of the side intensity spots (see also [Supplementary Video 1](#)).

Suppose a multi-ring structure is illuminated by an arbitrary optical beam with a complex amplitude  $u(\mathbf{r}, 0)$ . A straightforward generalization of the result of the previous section yields

$$\Psi(\mathbf{r}, z) = \frac{1}{2}u(\mathbf{r}, z) + \frac{1}{4N} \sum_{m=1}^M \sum_{n=1}^{2N_m} e^{-i2\pi z/z_{Tm}} e^{i2\pi \nu_m r \cos(\theta - \varphi_n^{(m)})} \times u(\mathbf{r}_n^{(m)}, z), \quad (18)$$

where  $\mathbf{r}_n^{(m)} = \mathbf{r} - \lambda z \mathbf{f}_n^{(m)}$  and  $z_{Tm} = 2\Lambda_m^2/\lambda$ . For the special case of a Gaussian incident beam, we have

$$\Psi(\mathbf{r}, z) = \frac{1}{2}u_G(r, z) + \frac{1}{4N} \sum_{m=1}^M \sum_{n=1}^{2N_m} e^{-i2\pi z/z_{Tm}} e^{i2\pi \nu_m r \cos(\theta - \varphi_n^{(m)})} \times u_G(r_n^{(m)}, z), \quad (19)$$

where  $u_G$  is given by equation (11).

#### 4.1. Double-ring APSs

The transmittance of any double-ring APS reads

$$t_{2N}^{(2)}(\mathbf{r}) = \frac{1}{2} + \frac{1}{2N} \sum_{n=1}^{N_1} \cos(2\pi \mathbf{f}_n^{(1)} \cdot \mathbf{r}) + \frac{1}{2N} \sum_{n=1}^{N_2} \cos(2\pi \mathbf{f}_n^{(2)} \cdot \mathbf{r}), \quad (20)$$

where  $N = N_1 + N_2$ . To demonstrate the versatility of our design, we created a structure with impulses arranged in a hexagram pattern (also known as David's star). This was achieved by setting  $N_1 = N_2 = 3$ ,  $\Lambda_2 = \Lambda_1/\sqrt{3}$ ,  $\alpha_1 = 0$ , and

$\alpha_2 = \pi/6$ . In figure 5(a), we illustrate the transmittance of this structure. As the impulse comb forms a 2D lattice, the transmittance is a 2D periodic function, see [22, 23]. In figures 5(b) and (c), we show the corresponding diffraction patterns of the structure illuminated by a Gaussian beam with  $\lambda = 532$  nm and  $w_0 = 2.5$  mm at  $z = z_R/4$ . To increase the visibility of the side intensity spots, we employ a logarithmic color scale in (b) and the remove the central diffraction order in (c). Furthermore, in [Supplementary Video 1](#), we showcase the evolution of the diffraction pattern as it propagates from  $z = 0$  to  $z = 5$  m.

As a further illustration, we construct a family of double-ring APSs with the impulses positioned at the vertices and mid-points of regular polygon sides. We then set  $N_1 = N_2 = N/2$ ,  $\Lambda_2 = \Lambda_1 \cos(\pi/N)$ ,  $\alpha_1 = 0$ , and  $\alpha_2 = \pi/N$  based on basic geometric principles. We depict the transmittance of these structures and the corresponding diffraction patterns under illumination by a Gaussian beam in figure 6.

#### 4.2. Triple-ring APSs

We introduce a family of APSs featuring impulses placed at the vertices and three equidistant points along the regular polygon sides. These impulses are distributed across three rings. However, the impulses on the second ring exhibit an irregular distribution. To achieve this structure, we construct an APS with four rings with the second and third rings sharing the same radius but corresponding to different  $\alpha$ 's. Using elementary geometric properties detailed in [appendix](#), we set  $N_1 = N_2 = N_3 = N_4 = N/4$ ,  $\Lambda_3 = \Lambda_2 = \frac{2\Lambda_1 \cos \vartheta}{\sqrt{1+3\cos^2 \vartheta}}$ ,  $\Lambda_4 = \Lambda_1 \cos \vartheta$ ,  $\alpha_1 = 0$ ,  $\alpha_2 = -\alpha_3 = \cot^{-1}(2 \cot \vartheta)$ , and  $\alpha_4 = \vartheta$  where  $\vartheta =$

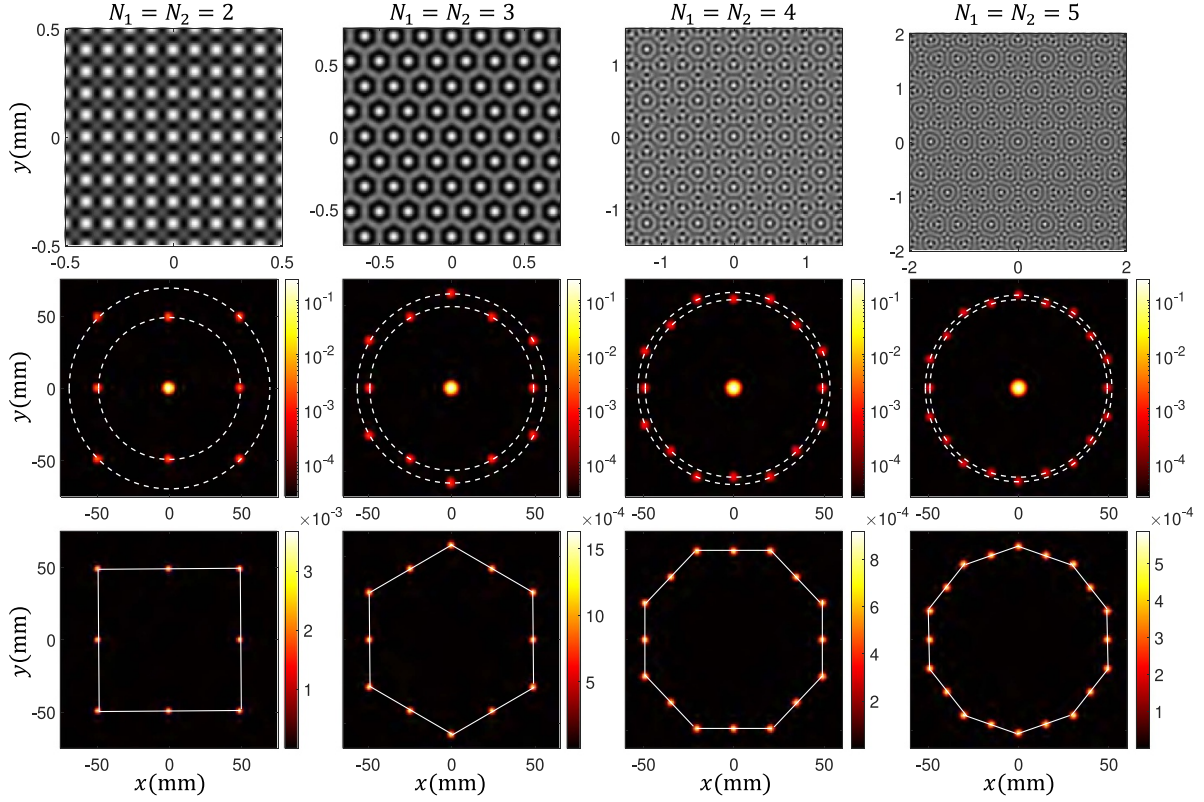


**Figure 6.** Top row: transmission function of double-ring APS with  $N_1 = N_2 = N/2$ ,  $\Lambda_2 = \Lambda_1 \cos(\pi/N)$ ,  $\alpha_1 = 0$ , and  $\alpha_2 = \pi/N$ . Middle and bottom rows: diffraction pattern of a Gaussian beam with  $\lambda = 532$  nm and  $w_0 = 2.5$  mm at a distance  $z = z_R/4$  from this structure. In the middle row, a logarithmic color scale is used. In the bottom row, the central diffraction order has been removed to increase the visibility of the side intensity spots.

$\frac{\pi}{2N_1}$ . We exhibit the transmittance and corresponding diffraction patterns of these structures illuminated by a Gaussian beam in figure 7. Additionally, [Supplementary Video 2](#) provides animation of the incident beam evolution on propagation from  $z = 0$  to  $z = 8$  m.

#### 4.3. Quadruple-ring APSs

To further illustrate the power of our general formulation, we consider additional examples, including two families of quadruple-ring APS structures. In the first instance, the impulses are positioned at the vertices and midpoints of hexagram sides. These impulses are distributed over four rings. However, the impulses on the third ring do not exhibit a regular pattern. For constructing the desired structure, we define an APS with five rings where the third and fourth rings have the same radius but different values of  $\alpha$ . Using the results of [appendix](#), we set  $N_1 = N_2 = N_3 = N_4 = N_5 = 3$ ,  $\Lambda_2 = \Lambda_1 \cos(\pi/6)$ ,  $\Lambda_3 = \Lambda_4 = \Lambda_1 \sqrt{3}/7$ ,  $\Lambda_5 = \Lambda_1/2$ ,  $\alpha_1 = \alpha_5 = \pi/6$ ,  $\alpha_2 = 0$ ,  $\alpha_3 = \cot^{-1}(5/\sqrt{3})$ , and  $\alpha_4 = -\cot^{-1}(5/\sqrt{3})$ . In figure 8, we display the transmittance of the structure and corresponding diffraction patterns illuminated by a Gaussian beam. Moreover, [Supplementary Video 3](#) shows animation of beam evolution from  $z = 0$  to  $z = 5$  m.

We introduce a second family of quadruple-ring structures with the impulses positioned at the vertices and midpoints of two concentric regular polygon sides. In this regard, we set

$N_1 = N_2 = N_3 = N_4 = N/4$ ,  $\Lambda_1 = 0.2$  mm,  $\Lambda_2 = \Lambda_1 \cos(\vartheta)$ ,  $\Lambda_3 = 0.1$  mm,  $\Lambda_4 = \Lambda_3 \cos(\vartheta)$ ,  $\alpha_1 = \alpha_3 = 0$ , and  $\alpha_2 = \alpha_4 = \vartheta$  where  $\vartheta = \frac{\pi}{2N_1}$ . In figure 9, we illustrate the transmittance and resulting diffraction pattern of the structure illuminated by a Gaussian beam.

## 5. Experiments

We now validate theoretical predictions through a series of experiments to realize beam splitting by DOEs. Our approach involves printing transmission functions of various multi-ring APSs onto plastic sheets. Alternatively, sheet glasses can be used instead, offering higher resolution but at a greater monetary and preparation time cost.

Figure 10 illustrates our experimental configuration for implementing different APSs. These structures are illuminated using a Gaussian beam generated by a neodymium-doped yttrium aluminum garnet (ND:YAG) diode-pumped laser of wavelength  $\lambda = 532$  nm. After passing through a spatial filter and a pinhole, the laser beam is collimated using a lens with a 10 cm focal length. The resulting beam impinges on an APS, as depicted in the inset of the figure. To capture Fraunhofer diffraction patterns, we employ another lens and a Nikon D7200 camera. For high-resolution, aberration-free images, we remove the imaging lens from the camera setup and directly record the diffraction pattern onto the camera sensor. By

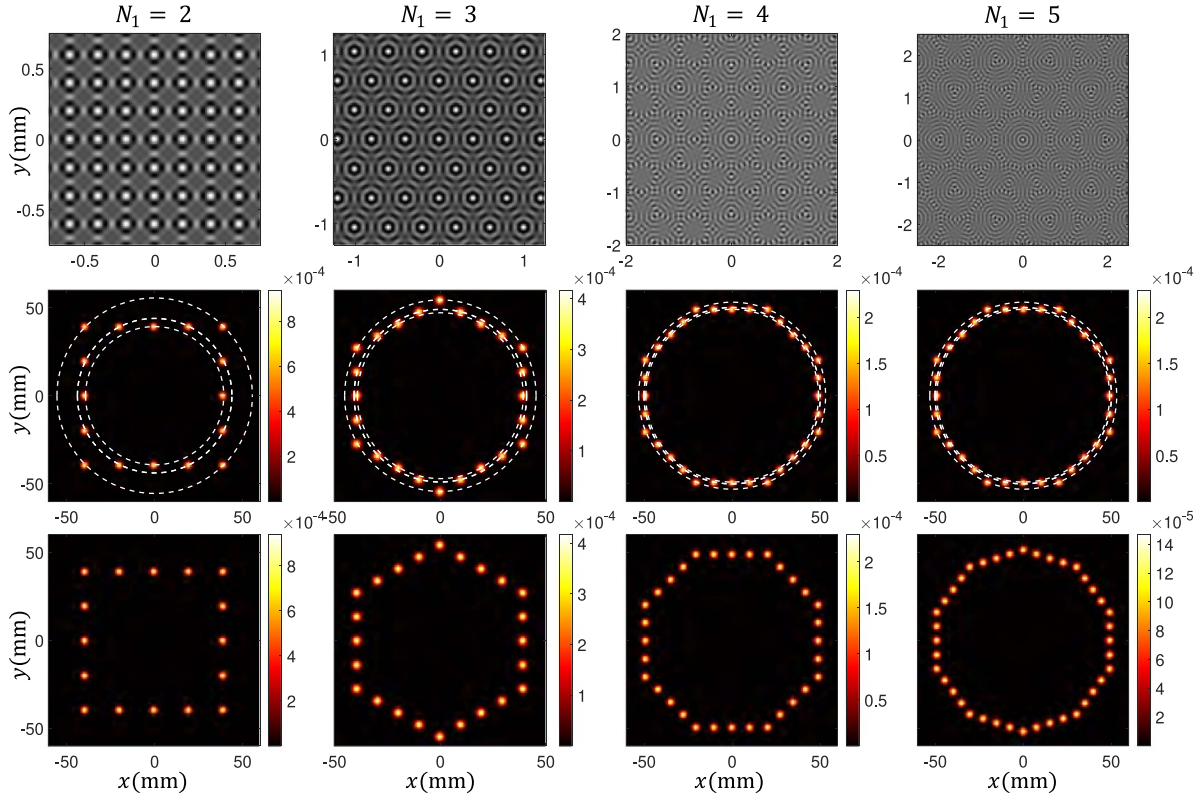


**Figure 7.** Top row: transmission function of multi-ring structures with  $N_1 = N_2 = N_3 = N_4 = N/4$ ,  $\Lambda_3 = \Lambda_2 = \frac{2\Lambda_1 \cos \vartheta}{\sqrt{1+3\cos^2 \vartheta}}$ ,  $\Lambda_4 = \Lambda_1 \cos \vartheta$ ,  $\alpha_1 = 0$ ,  $\alpha_2 = -\alpha_3 = \cot^{-1}(2 \cot \vartheta)$ , and  $\alpha_4 = \vartheta$  where  $\vartheta = \frac{\pi}{2N_1}$ . Middle and bottom rows: diffraction pattern of a Gaussian beam with  $\lambda = 532$  nm and  $w_0 = 2.5$  mm at a distance  $z = z_R/4$  from this structure. In the middle and bottom rows, the central diffraction order has been removed to increase the visibility of the side intensity spots (see also [Supplementary Video 2](#)).

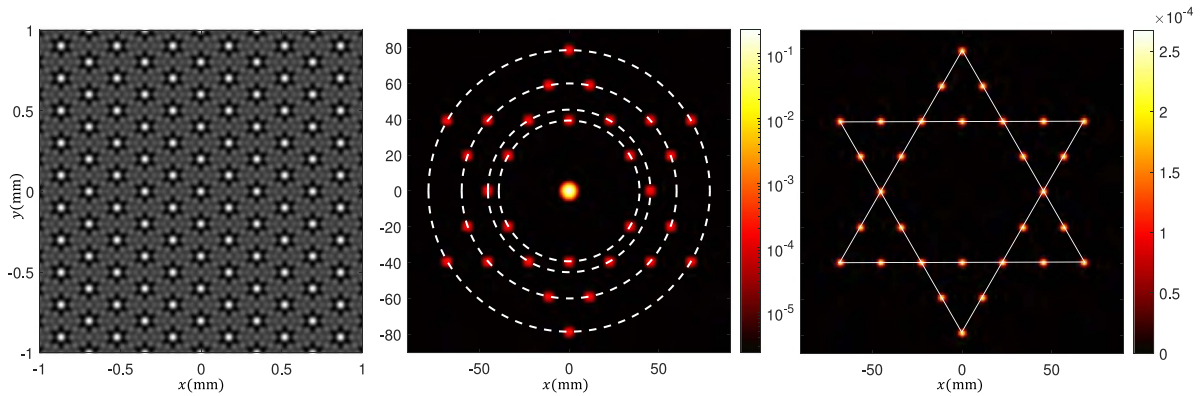


**Figure 8.** First column: transmission function of a multi-ring APS with  $N_1 = N_2 = N_3 = N_4 = N_5 = 3$ ,  $\Lambda_2 = \Lambda_1 \cos(\pi/6)$ ,  $\Lambda_3 = \Lambda_4 = \Lambda_1 \sqrt{3/7}$ ,  $\Lambda_5 = \Lambda_1/2$ ,  $\alpha_1 = \alpha_5 = \pi/6$ ,  $\alpha_2 = 0$ ,  $\alpha_3 = \cot^{-1}(5/\sqrt{3})$ , and  $\alpha_4 = -\cot^{-1}(5/\sqrt{3})$ . Second and third columns: diffraction pattern of a Gaussian beam with  $\lambda = 532$  nm and  $w_0 = 2.5$  mm at a distance  $z = z_R/5$  from this structure. In the second column, a logarithmic color scale is used, in the third column, the central diffraction order has been removed to increase the visibility of the side intensity spots (see also [Supplementary Video 3](#)).

further removing the Fourier transforming lens (Lens 2) in the far-field setup, we achieve even higher-resolution diffracted patterns directly on the camera sensor.

In figure 11 we depict both calculated and experimentally recorded Fraunhofer diffraction patterns of a single-ring APS with  $N = 3$  and  $\Lambda = 0.1$  mm. The APS is illuminated by a Gaussian beam of wavelength  $\lambda = 532$  nm and beam

waist diameter  $w_0 = 1.5$  mm. These diffraction patterns are observed under propagation near the focal plane of the Fourier transforming lens. Here, the evaluated diffracted intensities are normalized to the incident intensity peak on the structures, resulting in color bars with a maximum value of one immediately past the structures. Various diffraction orders separate on propagation and take on the spatial profile of the incident

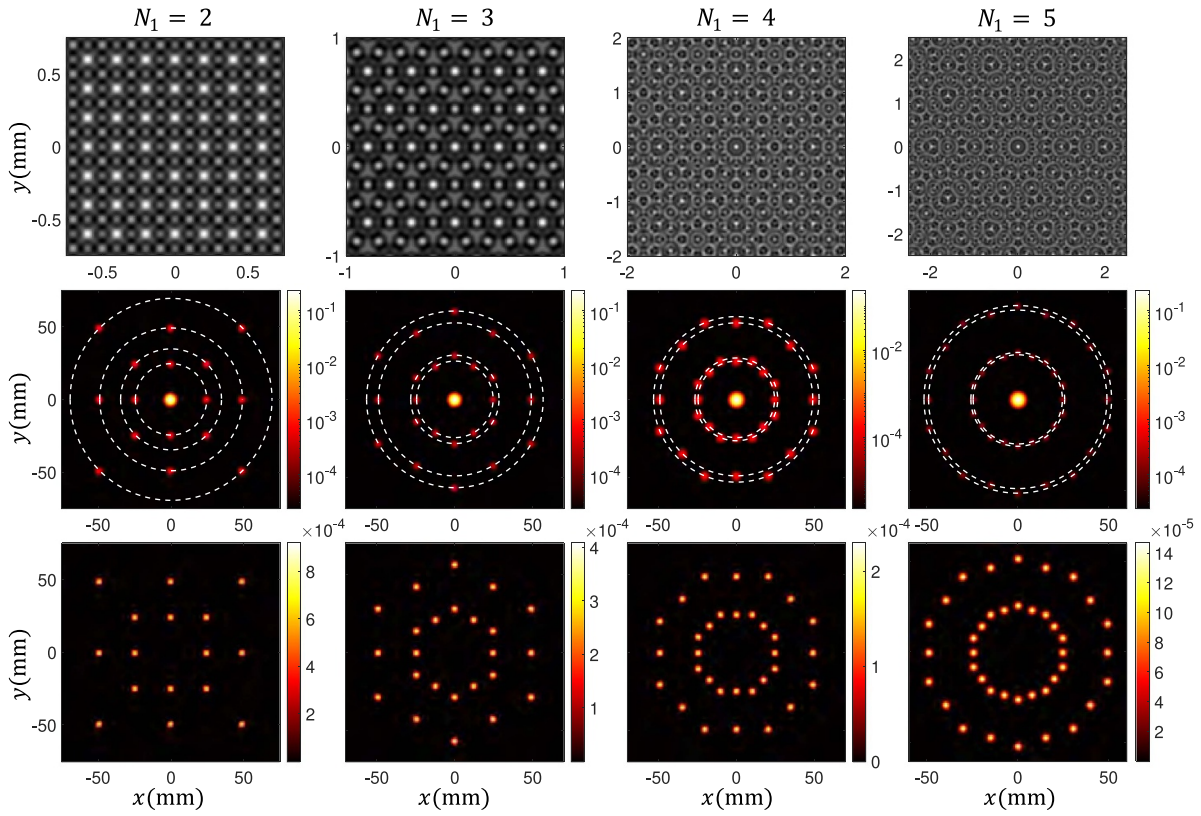


**Figure 9.** Top row: transmission function of four-ring APS structures with  $N_1 = N_2 = N_3 = N_4 = N/4$ ,  $\Lambda_1 = 0.2$  mm,  $\Lambda_2 = \Lambda_1 \cos(\vartheta)$ ,  $\Lambda_3 = 0.1$  mm,  $\Lambda_4 = \Lambda_3 \cos(\vartheta)$ ,  $\alpha_1 = \alpha_3 = 0$ , and  $\alpha_2 = \alpha_4 = \vartheta$  where  $\vartheta = \frac{\pi}{2N_1}$ . Middle and bottom rows: diffraction pattern of a Gaussian beam with  $\lambda = 532$  nm and  $w_0 = 2.5$  mm at a distance  $z = z_R/4$  from this structure. In the middle row, a logarithmic color scale is used. In the bottom row, the central diffraction order has been removed to increase the visibility of the side intensity spots.

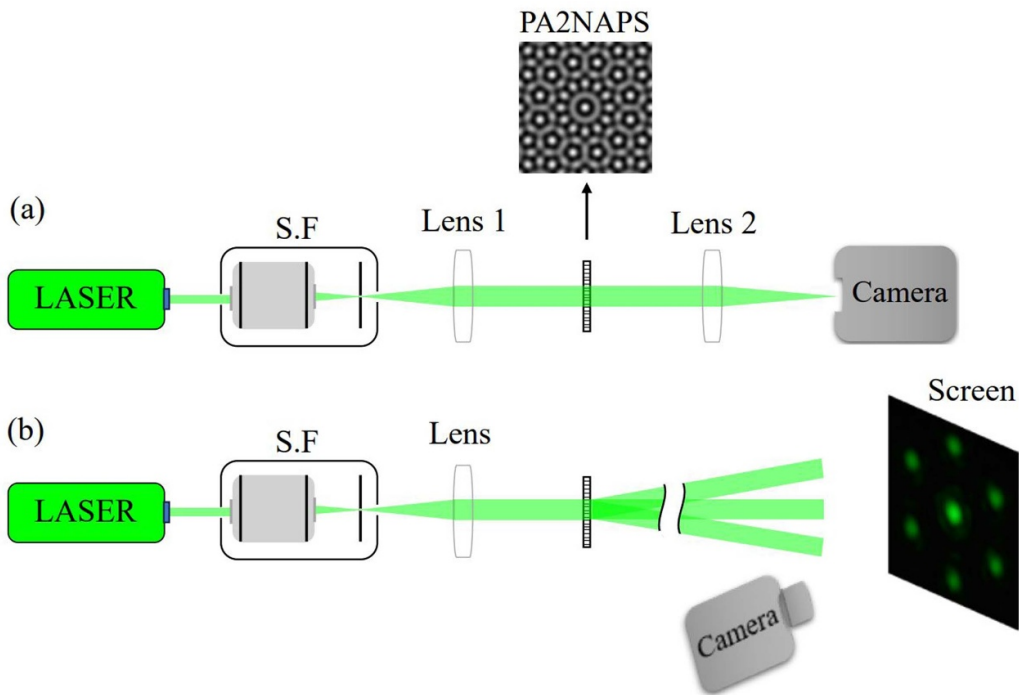


**Figure 10.** Experimental setups used for recording APS diffraction patterns. (a) Fraunhofer and (b) far-field diffraction pattern setups; S.F. stands for a spatial filter.

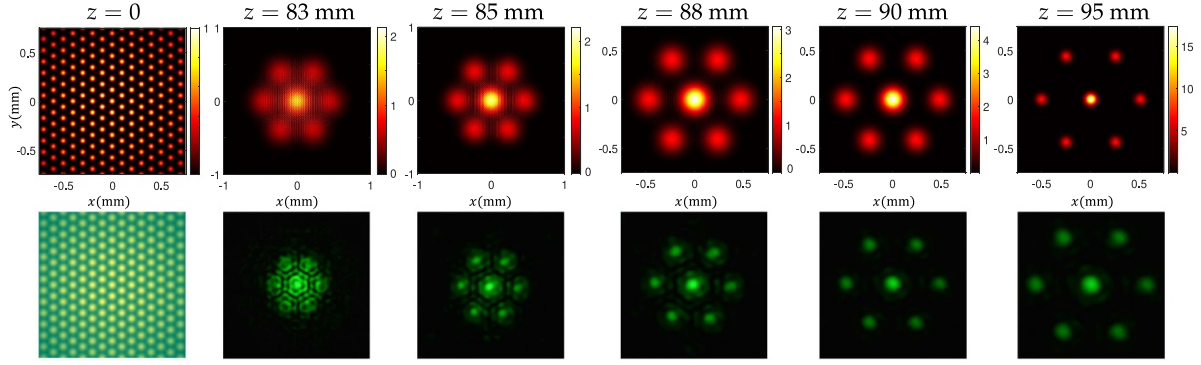


**Figure 11.** Top row: Calculated diffraction patterns; bottom row: Experimentally recorded diffraction patterns of a single-ring APS with  $N = 3$  and  $\Lambda = 0.1$  mm. The APS is illuminated by a Gaussian beam with  $\lambda = 532$  nm and a beam waist diameter of  $w_0 = 1.5$  mm. These patterns are observed under propagation near the focal plane of the Fourier transforming lens with  $f = 10$  cm.

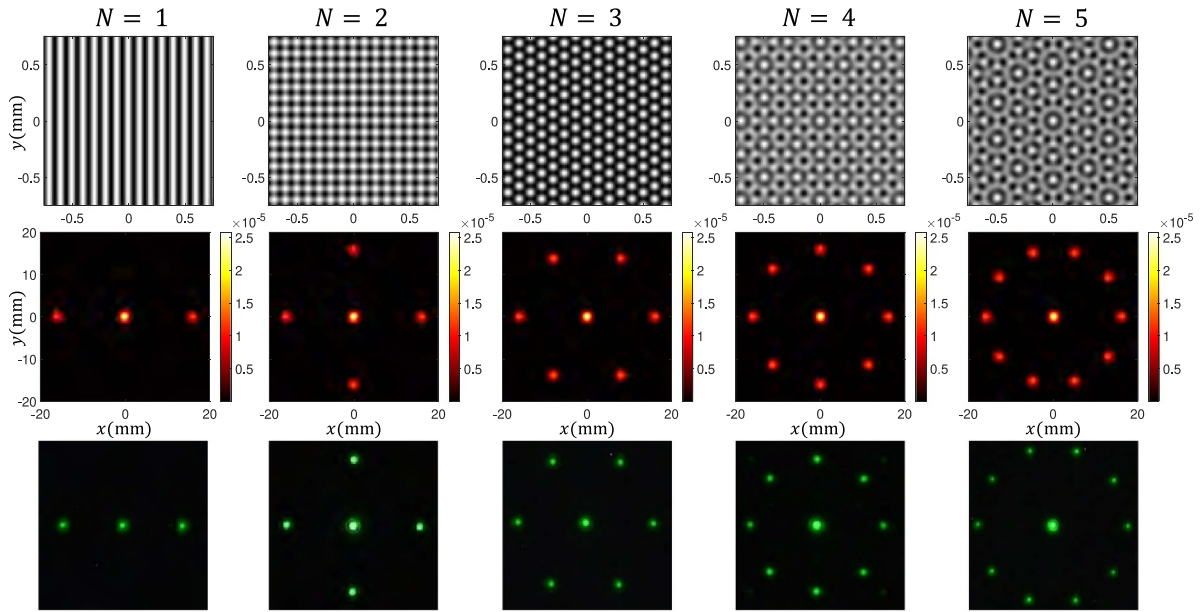


**Figure 12.** Top row: Transmission functions of several single-ring APSs with  $\Lambda = 0.1$  mm and varying values of  $N$ . Middle and bottom rows: Corresponding calculated (middle row) and experimentally recorded (bottom row) far-field diffraction patterns observed at a distance of  $z = 3$  m from APSs. These patterns result from illuminating the APSs with a Gaussian beam having a wavelength of  $\lambda = 532$  nm and a beam waist diameter of  $w_0 = 1.5$  mm.

beam. However, the intensity maxima are boosted by a focusing lens.

In figure 12 we show the transmittances of several single-ring APSs with  $\Lambda = 0.1$  mm and variable  $N$ . Additionally, the figure showcases both calculated and experimentally recorded far-field diffraction patterns observed at  $z = 3$  m from the structures. These diffraction patterns emerge from illuminating the APSs with the same Gaussian beam but of a different waist diameter  $w_0 = 2.5$  mm.

In figure 13 we exhibit transmittances of several double- and triple-ring APSs with  $\Lambda = 0.1$  mm, and the corresponding calculated and experimentally recorded far-field diffraction patterns at  $z = 3$  m from the structures. These diffraction patterns arise from illuminating the APSs with the same Gaussian beam as in figure 12. We find excellent agreement between the theory (red) and experiment (green).

As observed in the bottom row of figure 13, high-order diffraction patterns are evident. This phenomenon arises due to the non-sinusoidal, binary-like transmission profiles of the fabricated APSs, which differ from the idealized sinusoidal profiles assumed in the theoretical model. While sinusoidal transmission profiles predominantly generate zero and first diffraction orders, binary-like profiles result in additional higher-order diffraction patterns. This deviation underscores the impact of the transmission profile shape on the diffraction behavior of APSs.

To provide a deeper understanding of the efficiency and behavior of APSs, we conducted a detailed comparison between the theoretical predictions and experimental results across various configurations. From the theoretical stand point for pure amplitude APSs with the transmission function given in equation (17), the power share of each side intensity impulse is calculated as  $\frac{1}{(2N+1)(2N)}$  of the transmitted beam power,

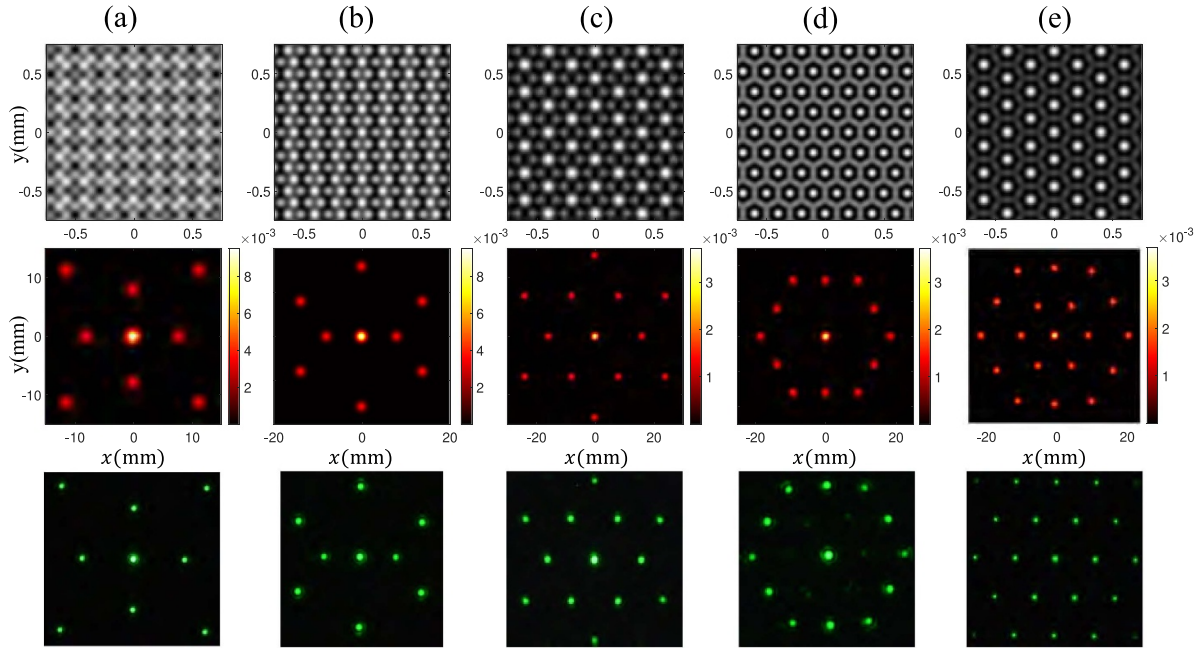


**Figure 13.** Top row: Transmission functions of various double-ring structures (columns a–d) and a triple-ring APS (column e). Middle and bottom rows: Corresponding calculated (middle row) and experimentally recorded (bottom row) diffraction patterns observed at a distance of  $z = 3$  m from APSs. These patterns result from illuminating APSs with a Gaussian beam featuring a wavelength of  $\lambda = 532$  nm and a beam waist diameter of  $w_0 = 2.5$  mm.

where  $2N$  represents the total number of impulses excluding the zero-diffraction order. The central intensity impulse receives a power share of  $\frac{2N}{2N+1}$ , and the ratio of transmitted to incident power is given by  $\frac{2N+1}{8N}$ . As a result, the theoretical power transmitted into each side spot is  $\frac{1}{16N^2}$  of the incident power.

For comparison, spatial light modulators (SLMs) illuminated by plane or Gaussian waves generally exhibit much lower efficiency. A two-dimensional periodic structure implemented on an SLM distributes less than 1% of the incident beam power to each diffraction order, even without amplitude or phase shaping. When amplitude or phase modulation is applied, the redistribution of transmitted power further reduces the intensity in the desired secondary diffraction orders. In contrast, pure amplitude APSs provide a practical and efficient alternative, consistently achieving a transmitted-to-incident power ratio exceeding 0.25, as predicted by  $\frac{2N+1}{8N}$ . This advantage demonstrates the superior energy efficiency of APSs compared to SLMs for beam-shaping applications (for further details, see [6]).

To illustrate this, we investigated in detail the diffraction efficiency of two different pure amplitude APSs: one with a single circle of 8 impulses ( $N = 4$ ) and another with two circles, each containing 8 impulses ( $N_1 = N_2 = 4$ ). Figure 14 shows the recorded images of the experimentally generated impulses from these APSs when illuminated by a Gaussian beam. The diffraction patterns were formed on a diffuser plane located at the focal plane of a lens with a focal length  $f = 100$  cm. The diffraction patterns, representing the impulses, were captured using a Nikon D7200 camera. To measure the power carried by each diffraction order, we replaced the

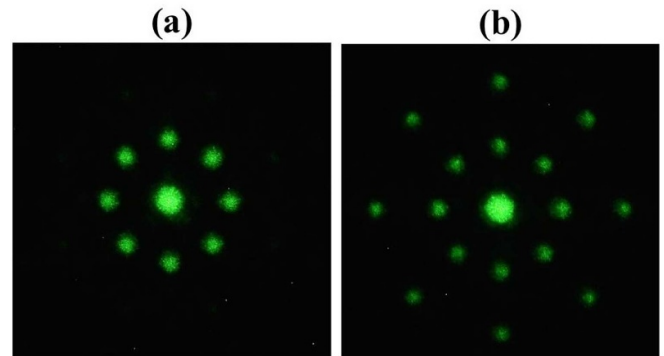


**Figure 14.** Recorded images of experimentally generated impulses from two pure amplitude APSs illuminated by a Gaussian beam. The spectrum of the first APS consists of a single circle with 8 impulses ( $N = 4$ ), while the second APS features two circles, each containing 8 impulses ( $N_1 = N_2 = 4$ ). Diffraction patterns were captured on a diffuser plane at the focal plane of a lens with  $f = 100$  cm, using a Nikon D7200 camera.

diffuser with an iris diaphragm, allowing only one diffraction order to pass through. A power meter (Coherent LM-P10i Laser Detector) was then used to measure the power carried by this order. For the first APS, with one circle and 8 impulses, the experimentally measured mean power across the first eight diffraction orders was  $P_n = (76.89 \pm 1.98) \mu\text{W}$  for an incident power  $P_{in} = 7.51$  mW. The power directed into the zero-order diffraction was  $P_0 = 559 \mu\text{W}$ . For the second APS, which had impulses over two circles, the experimentally measured mean power across the eight diffraction orders of the

first circle was  $P_n = (48.66 \pm 0.58) \mu\text{W}$  for the same incident power  $P_{\text{in}} = 7.51 \text{ mW}$ , with the power directed into the zero-order diffraction  $P_0 = 661 \mu\text{W}$ . For the second circle, the mean power across the eight diffraction orders was  $P_n = (39.11 \pm 0.33) \mu\text{W}$ .

These measurements include error values calculated from the measurements of the side impulses in each respective circle. Both experimental values exceeded the theoretically predicted power distributions and were significantly higher than those obtained from identical structures implemented on a commercial SLM, which yielded much lower power distributions.

We repeated the same experiments using a commercial SLM (3 M X50, resolution:  $1024 \times 768$ , display size: 0.7 in, polysilicon LCD). The same APS structures were implemented on the SLM, and measurements were taken using the same methodology described above. For the first APS, the experimentally measured mean power across the eight side diffraction orders was  $P_n = (1207 \pm 37) \text{ nW}$  for an incident power of  $P_{\text{in}} = 7.79 \text{ mW}$ . The power directed into one of the diffraction orders of the SLM was  $P_0^{\text{SLM}} = 60.6 \mu\text{W}$  when no structure was implemented on the SLM. After implementing the first APS structure, the total power in each diffraction order of the SLM was  $P_0^{\text{SLM}} = 54.7 \mu\text{W}$ , and the power directed into the zero-order diffraction of the APS structure was  $P_0^{\text{APS}} = 34.9 \mu\text{W}$ . For the second APS implemented on the SLM, the experimentally measured mean power across the eight diffraction orders of the first circle was  $P_n = (522 \pm 12) \text{ nW}$  for the same incident power of  $P_{\text{in}} = 7.79 \text{ mW}$ , and the mean power across the eight diffraction orders of the second circle was  $P_n = (380 \pm 18) \text{ nW}$ .

As observed, the power directed to each of the side diffraction orders for the first APS ( $P_n = 76.89 \mu\text{W}$ ) is 64 times greater than the corresponding power for the same diffraction order generated by the SLM ( $P_n^{\text{SLM}} = 1207 \text{ nW}$ ). Similarly, for the first circle of the second APS, the power directed to each side diffraction order ( $P_n = 48.66 \mu\text{W}$ ) is 93 times greater than that for the same order produced by the SLM ( $P_n^{\text{SLM}} = 522 \text{ nW}$ ). Finally, for the second circle of the second APS, the power directed to each side diffraction order ( $P_n = 39.11 \mu\text{W}$ ) is 103 times greater than the power of the corresponding diffraction order generated by the SLM ( $P_n^{\text{SLM}} = 380 \text{ nW}$ ).

An intriguing observation during the experiments was that the side diffraction orders carried more power than theoretically predicted. For instance, for the first APS considered above, we experimentally measured  $P_n = 48.66 \mu\text{W}$ ; however, in theory, for an incident power  $P_{\text{in}} = 7.51 \text{ mW}$ , using the relation  $\frac{P_n}{P_{\text{in}}} = \frac{1}{256}$ , we evaluate  $P_n = 29.33 \mu\text{W}$ . This deviation arises because the fabricated APSs exhibit non-sinusoidal, binary-like transmission profiles instead of the idealized sinusoidal profiles assumed in the theoretical model. Unlike sinusoidal profiles, which tend to concentrate more power in the zeroth diffraction order, binary-like profiles result in a more balanced power distribution across the diffraction orders. This characteristic explains the higher-than-expected amplitudes of the surrounding diffraction spots in the experimental results. A comprehensive investigation into this effect is planned as part of our future research endeavors.

## 6. Conclusion

In this work, we introduced a new class of DOEs belonging to the broader category of APSs. These structures are uniquely characterized by their multi-ring spatial spectra, offering a high degree of design flexibility through the parameters ( $M, N_m, \nu_m, \alpha_m$ ), which define the number of rings, the number of impulses per ring, the radii of the rings, and the angular positioning of impulses, respectively.

We developed a general mathematical framework to describe the diffraction of optical beams by these structures and applied it to analyze the interaction of Gaussian beams with APSs. Our results demonstrated that the diffraction patterns of these elements, observed either at large distances or near the focal plane of a Fourier lens, consist of  $2N$  high-intensity Gaussian beamlets with equal power distribution. These findings were validated both theoretically and experimentally, underscoring the robustness of our approach.

The versatility of APS designs was illustrated through examples featuring double-, triple-, and quadruple-ring spatial spectra, highlighting the potential of these elements in advanced optical applications. Specifically, their ability to produce structured diffraction patterns with precise power distribution and spatial arrangement opens up opportunities in three-dimensional optical trapping, beam splitting, and other domains requiring intricate light manipulation.

Future work could explore further optimization of APS designs for specific applications, as well as the extension of the proposed framework to accommodate other types of structured beams and wavefronts. Additionally, investigating the impact of fabrication tolerances on the performance of these elements could help bridge the gap between theory and practical implementation.

In conclusion, this study establishes APSs as a powerful tool in the design of DOEs, with broad implications for structured light applications, beam splitting and shaping, optical trapping technologies, and microscopy.

## Data availability statement

No new data were created or analysed in this study.

## Acknowledgment

This study was partially funded by the Institute for Advanced Studies in Basic Sciences (No. G2024IASBS12632), Center for International Scientific Studies and Collaboration (CISSC) of Iran (No. 4020667), and Natural Sciences & Engineering Research Council (NSERC) of Canada (No. RGPIN-2018-05497). The author Saifollah Rasouli would like to acknowledge Abdus Salam International Center for Theoretical Physics (ICTP), Trieste, Italy, for the Senior Associate Fellowship (No. 2018-2023). The author Davud Hebrri would like to acknowledge Izaak Walton Killam Postdoctoral fellowship.

**Conflict of interest**

The authors declare no conflicts of interest.

**Funding**

Institute for Advanced Studies in Basic Sciences (G2024IASBS12632); Center for International Scientific Studies and Collaboration (CISSC) of Iran (No. 4020667); Natural Sciences & Engineering Research Council (NSERC) of Canada (No. RGPIN-2018-05497).

**Appendix. Geometric analysis**

To achieve multiple impulses along the sides of a polygon or the triangles of a Star of David, maintaining equal distances, we present the following calculations. This appendix provides essential geometric theorems and calculations for constructing multi-ring APSs. We begin by reviewing fundamental geometric formulas related to a triangle and its median. Consider a standard triangle  $ABC$  and its median  $AM$ , see figure A1 (left), which connects the vertex  $A$  to the midpoint of the opposite side,  $M$ . The lengths of the median  $\overline{AM}$  can be obtained from Apollonius theorem as

$$\overline{AM} = \frac{1}{2} \sqrt{2(b^2 + c^2) - a^2}. \tag{A1}$$

where  $a$ ,  $b$ , and  $c$  respectively are the lengths of the sides opposite to the vertices  $A$ ,  $B$ , and  $C$ . We also have

$$\frac{\sin \hat{A}_2}{\sin \hat{A}_1} = \frac{c}{b}, \tag{A2}$$

for angles  $\hat{A}_1$  and  $\hat{A}_2$ . Considering  $\hat{A} = \hat{A}_1 + \hat{A}_2$ , we obtain

$$\cot \hat{A}_1 = \cot \hat{A} + \frac{c}{b \sin \hat{A}}. \tag{A3}$$

Using figure A1 (right), when  $ABC$  is a right triangle,  $\hat{B} = 90^\circ$ , it is easy to show that equations (A1) and (A3) reduces to

$$\overline{AM} = \frac{1}{2} \sqrt{b^2 + 3c^2}, \tag{A4a}$$

$$\cot \hat{A}_1 = 2 \cot \hat{A}. \tag{A4b}$$

where we used the Pythagorean theorem,  $b^2 = c^2 + a^2$ , and  $\cos \hat{A} = c/b$ .

Now let us use equation (A4) to construct the impulse comb of the structures in figure 7. Figure A2 schematically illustrates a single side of the impulse comb. Five impulses positioned along one side are depicted with solid points in the figure. Looking at this figure we refer to  $\cos \vartheta = \frac{\nu_1}{\nu_4}$  or equivalently  $\Lambda_4 = \Lambda_1 \cos \vartheta$ . By setting  $c = \nu_1$ ,  $b = \nu_4$ ,  $\overline{AM} = \nu_2$ ,  $\hat{A}_1 = \alpha_2$ , and  $\hat{A} = \vartheta$  in equation (A4) we have

$$\nu_4 = \frac{\sqrt{1 + 3 \cos^2 \vartheta}}{2 \cos \vartheta} \nu_1, \tag{A5a}$$

$$\cot \alpha_2 = 2 \cot \vartheta, \tag{A5b}$$

or equivalently

$$\Lambda_4 = \frac{2 \cos \vartheta}{\sqrt{1 + 3 \cos^2 \vartheta}} \Lambda_1, \tag{A6a}$$

$$\alpha_2 = \cot^{-1} (2 \cot \vartheta). \tag{A6b}$$

Here we use equations (A1) and (A3) to calculate characteristic parameters of the structure illustrated in figure 8. First, we present figure A3 highlighting a single segment of the impulse comb of the structure depicted in figure 8. Six impulses forming a single triangular segment of the impulse comb are depicted with solid points in the figure. As is apparent  $\nu_1 = \nu_2 \cos(\pi/6)$  and  $\nu_5 = 2\nu_1$  or equally  $\Lambda_2 = \Lambda_1 \cos(\pi/6)$  and  $\Lambda_2 = \Lambda_1/2$ . Furthermore, by setting  $a = c = \nu_2$ ,  $b = 2\nu_1$ ,  $\overline{AM} = \nu_3$ ,  $\hat{A}_1 = \alpha_3$ , and  $\hat{A} = \pi/6$  in equations (A1) and (A3) we obtain

$$\nu_3 = \sqrt{7/3} \nu_1, \tag{A7a}$$

$$\cot \alpha_3 = 5/\sqrt{3}, \tag{A7b}$$

or equally  $\Lambda_3 = \sqrt{3/7} \Lambda_1$  and  $\alpha_3 = \cot^{-1} (5/\sqrt{3})$ .

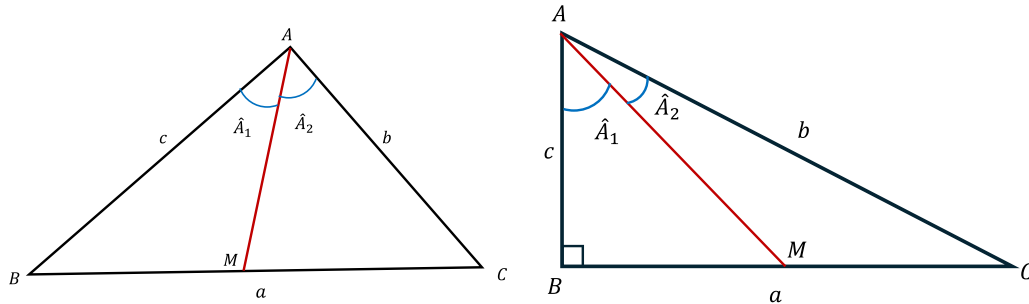


Figure A1. A typical triangle (left) and a right triangle (right) ABC and their medians AM.

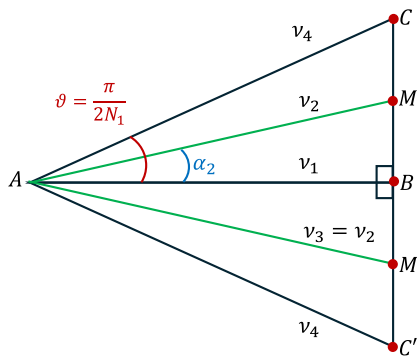


Figure A2. Schematic illustration: the impulses over the one side of impulse comb of the structures in figure 7. The zero-order impulse is positioned at vertex A, while the locations of the five impulses along one side of the impulse comb are marked as C, M, B, M', and C'.

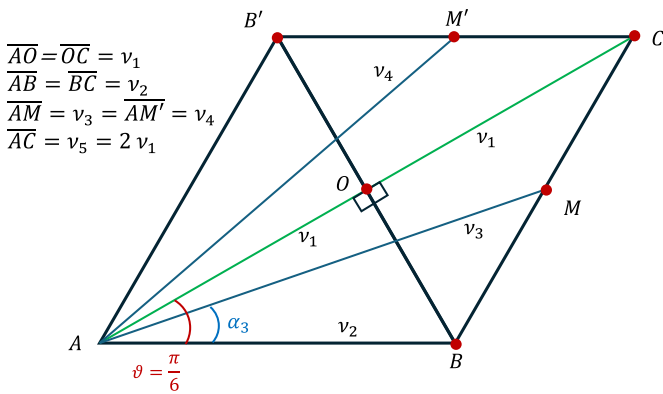


Figure A3. Schematic illustration highlighting a single segment of the impulse comb of the structure depicted in figure 8. Vertex A corresponds to the zero-order impulse, while B, B', and C represent the three vertices of a single triangular segment of the impulse comb.

ORCID iD

Saifollah Rasouli  <https://orcid.org/0000-0003-2703-8925>

References

[1] Hopkinson F and Rittenhouse D 1786 *Trans. Am. Phil. Soc.* **2** 201–6  
 [2] Von Fraunhofer J 1821 *Denkschr. Königlichen Akad. Wiss Zu München* **8** 3–76

[3] Gibson G, Courtial J, Padgett M J, Vasnetsov M, Pas’ko V, Barnett S M and Franke-Arnold S 2004 *Opt. Express* **12** 5448–56  
 [4] Khazaei A M, Hebri D and Rasouli S 2023 *Opt. Express* **31** 16361–79  
 [5] Zhang Q, He Z, Xie Z, Tan Q, Sheng Y, Jin G, Cao L and Yuan X 2023 *Photon. Insights* **2** R09–R09  
 [6] Moghadam P Y, Rasouli S, Hajizadeh F and Hebri D 2023 *Opt. Express* **31** 43490–505  
 [7] Loewen E G and Popov E 2018 *Diffraction Gratings and Applications* (CRC Press)  
 [8] Soifer V A, Doskolovich L, Golovashkin D, Kazanskiy N, Kharitonov S, Khonina S, Kotlyar V, Pavelyev V, Skidanov R and Solovyev V 2002 *Methods for Computer Design of Diffractive Optical Elements* (Wiley)  
 [9] Dickey F M 2018 *Laser Beam Shaping: Theory and Techniques* (CRC Press)  
 [10] Dammann H and Görtler K 1971 *Opt. Commun.* **3** 312–5  
 [11] Gori F, Santarsiero M, Vicalvi S, Borghi R, Cincotti G, Di Fabrizio E and Gentili M 1998 *Opt. Commun.* **157** 13–16  
 [12] Borghi R, Cincotti G and Santarsiero M 2000 *J. Opt. Soc. Am. A* **17** 63–67  
 [13] Romero L A and Dickey F M 2007 *J. Opt. Soc. Am. A* **24** 2296–312  
 [14] Rubin N A, Shi Z and Capasso F 2022 *Adv. Opt. Photonics* **13** 836–970  
 [15] Marco D, Sánchez-López M M, Cofré A, Vargas A and Moreno I 2019 *Opt. Express* **27** 14472–86  
 [16] Rajabalipanah H, Abdolali A, Shabanpour J, Momeni A and Cheldavi A 2019 *ACS Omega* **4** 14340–52  
 [17] Gori F, Martinez-Herrero R, Korotkova O, Piquero G, De Sande J, Schettini G, Frezza F and Santarsiero M 2024 *J. Opt. Soc. Am. A* **41** 510–5  
 [18] Porfirev A P and Khonina S N 2017 *Opt. Express* **25** 18722–35  
 [19] Ruffato G, Girardi M, Massari M, Mafakheri E, Sephton B, Capaldo P, Forbes A and Romanato F 2018 *Sci. Rep.* **8** 10248  
 [20] Bohr H 1947 *Almost Periodic Functions* (Chelsea Publishing Company Reprint of the Original 1932 edn Published by Hafner Publishing Company)  
 [21] Besicovitch A S and Besicovitch A S 1954 *Almost Periodic Functions* vol 4 (Dover)  
 [22] Amidror I and Amidror I 2007 *The Theory of the Moiré Phenomenon: Volume II: Aperiodic Layers* pp 157–86  
 [23] Hebri D and Rasouli S 2019 *J. Opt. Soc. Am. A* **36** 253–63  
 [24] Samadzadeh M, Rasouli S, Hebri D and Ponomarenko S A 2024 *Appl. Phys. Lett.* **124** 1–6  
 [25] Siegman A E 1986 *Lasers* (University Science Books)